

## ARTICLE OPEN

# Mass fabrication and superior microwave absorption property of multilayer graphene/hexagonal boron nitride nanoparticle hybrids

Yongqing Bai<sup>1,2</sup>, Bo Zhong<sup>3</sup>, Yuanlie Yu<sup>1,2</sup>, Meng Wang<sup>1,3</sup>, Jing Zhang<sup>1,4</sup>, Bin Zhang<sup>1</sup>, Kaixiong Gao<sup>1</sup>, Aimin Liang<sup>1</sup>, Chunyu Wang<sup>3</sup> and Junyan Zhang<sup>1,2</sup>

Graphene has been regarded as a promising candidate in microwave absorption field but still faces some major challenges, including the limitation of mass production and poor impedance matching. Here, we demonstrate a simple approach to fabricate multilayer graphene in a kilo-mass/hour ( $\geq 2.5$  kg/h) scale through an oxidation-thermal expansion-air convection shearing process. The subsequent incorporation of hexagonal boron nitride nanoparticles (*h*-BNNPs) can effectively tailor the dielectric and magnetic properties of the as-obtained multilayer graphene, which can significantly boost its microwave absorption performance. The as-obtained multilayer graphene/*h*-BNNP hybrid with 40 wt.% of *h*-BNNPs, exhibits extremely low reflection loss value of  $-67.35$  dB at 8.04 GHz when the absorber thickness is 3.29 mm, ranking it as one of the most attractive absorbers reported to date. Moreover, the multilayer graphene/*h*-BNNP hybrids possess low densities less than  $0.45$  g/cm<sup>3</sup>, making them very attractive for practical microwave absorption application.

npj 2D Materials and Applications (2019)3:32; <https://doi.org/10.1038/s41699-019-0115-5>

## INTRODUCTION

Recently, severe electromagnetic microwave pollution induced by the rapid development of electronic information technologies including wireless data communications, satellite communications, radar detections, self-concealing, as well as microwave heating,<sup>1–3</sup> has aroused global concerns. To eliminate the detriment of this electromagnetic microwave pollution on human beings and wildlife, highly efficient microwave absorption materials are required. Besides, stealth technology is also promoting the development of these microwave absorption materials. However, searching for ideal microwave absorption materials is challengeable, because of the critical indispensable requirement, such as good mechanical strength, light weight, low loading rate, decent chemical corrosion resistance and high thermal stability.<sup>4,5</sup> Recently, graphene-based nanocomposites have attracted great interest in exploring efficient microwave absorption materials due to their exceptional chemical and physical properties such as low density, good chemical inertness, and excellent mechanical properties.<sup>6–9</sup> However, two major issues still need to be solved for their practical application, including the limitation of large-scale fabrication and poor impedance matching that resulted from the high dielectric constant and nonmagnetic property of graphene. As for the mass production of graphene, various strategies have been explored, such as mechanical exfoliation techniques,<sup>10</sup> chemical vapor deposition,<sup>11</sup> solid-state carbon source deposition,<sup>12</sup> solution exfoliation,<sup>13</sup> nanotube splitting and unzipping,<sup>14,15</sup> and chemical reduction of graphene oxide (GO).<sup>16</sup> On the other

hand, hybridizing dielectric/magnetic nanostructures with graphene has been considered a facial way to tune the dielectric constant and nonmagnetic property of graphene, which would dramatically boost its microwave absorption performance. In this regard, diverse dielectric/magnetic nanostructure/graphene materials have been synthesized, such as graphene@SiC composite,<sup>17,18</sup> Fe<sub>3</sub>O<sub>4</sub>-Fe/graphene composite,<sup>19</sup> Fe<sub>3</sub>O<sub>4</sub>/graphene composite,<sup>20</sup> NiFe<sub>2</sub>O<sub>4</sub>/graphene hybrid,<sup>21</sup> SiO<sub>2</sub>@Fe<sub>3</sub>O<sub>4</sub> nanorod array/graphene architecture,<sup>22</sup> and porous graphene micro flowers.<sup>23</sup> Despite this sign of progress, the current state-of-the-art graphene-based hybrids still suffer from high cost, complicated preparation process, high densities, as well as bad chemical corrosive resistance, hindering their full application as microwave absorption materials.

Hexagonal boron nitride (*h*-BN) is a structurally analog to graphite with almost the same crystal lattice parameters.<sup>24</sup> As a result, *h*-BN nanomaterials show many similar properties as graphitic materials, such as low density, high mechanical strength, good chemical corrosive resistance, excellent oxidation resistance, good lubricating property and outstanding thermal conductivity.<sup>25–32</sup> However, compared with graphitic materials, *h*-BN nanomaterials also possess superior electrical resistivity of  $10^{-16}$ – $10^{-18}$  Ω·cm and wide band gap over 6.0 eV.<sup>33,34</sup> Interestingly, these superior electrical resistivity and wide band gap of *h*-BN nanomaterials are beneficial to tune the dielectric property of graphene through hybridizing of them.<sup>35,36</sup> More importantly, the formation of the graphene/*h*-BN nanomaterial hybrids can keep the low density, high mechanical strength, good chemical

<sup>1</sup>R&D Center of Lubricating and Protecting Materials, Lanzhou Institute of Chemical Physics, Chinese Academy of Sciences, 730000 Lanzhou, People's Republic of China; <sup>2</sup>Center of Materials Science and Optoelectronics Engineering, University of Chinese Academy of Sciences, 100049 Beijing, People's Republic of China; <sup>3</sup>School of Materials Science and Engineering, Harbin Institute of Technology at Weihai, 264209 Weihai, People's Republic of China and <sup>4</sup>School of Physics, State Key Laboratory of Crystal Materials, Shandong University, 250100 Jinan, People's Republic of China

Correspondence: Yuanlie Yu (yuanliehl@licp.cas.cn) or Junyan Zhang (zhangjunyan@licp.cas.cn)

These authors contributed equally: Yongqing Bai, Bo Zhong, Yuanlie Yu

Received: 1 April 2019 Accepted: 16 July 2019

Published online: 23 August 2019

corrosive, and excellent oxidation resistance of graphene and *h*-BN nanomaterials. Also, the interface effect appeared between graphene and *h*-BN nanomaterials will cause polarization to generate magnetism,<sup>37–40</sup> which is also critical for enhancing the microwave absorption property of graphene.

Herein, the multilayer graphene/*h*-BN nanoparticle (MG/*h*-BNNP) hybrids are fabricated through two simple steps. The first step is the mass fabrication of multilayer graphene in kilo-mass/hour scale, which involves a simple oxidation-thermal expansion-air convection shearing process with natural graphite flakes as precursors. Then, these as-obtained multilayer graphene is subjected to a ball milling process with *h*-BNNPs to obtain the MG/*h*-BNNP hybrids. The morphology and composition of the samples were investigated by complementary imaging and spectroscopic technologies including X-ray diffraction (XRD), Raman spectrum, X-ray photoelectron spectroscopy (XPS), field emission scanning electronic microscopy (FESEM), transmission electron microscopy (TEM), high resolution transmission electron microscopy (HRTEM), energy dispersive X-ray spectroscopy (EDX), and atomic force microscopy (AFM). The magnetic property was investigated with a VSM magnetometer from Quantum Design. The microwave absorption properties were systematically evaluated by a vector network analyzer in transmission-reflection mode in the frequency range of 2–18 GHz. The as-obtained MG/*h*-BNNP hybrid based absorber with 40 wt.% of *h*-BNNPs exhibits extremely low reflection loss (RL) value of  $-67.35$  dB at 8.04 GHz, which is superior to most of the graphene or reduced graphene oxide (rGO) based absorbers reported in the literatures. The excellent microwave absorption performance makes the MG/*h*-BNNP hybrids promising for practical microwave absorption application.

## RESULTS

### Mass fabrication and characterization of multilayer graphene

The expandable graphite was prepared by the method reported in the literature<sup>41</sup> before exfoliation. In brief, the expandable graphite was fabricated by using  $\text{H}_2\text{SO}_4$ -graphite intercalation

composite, which could yield a high expansion volume via a thermal treatment (Fig. S1a–d) at 700 °C. This thermal treatment condition has been demonstrated as an effective way to complete expansion of  $\text{SO}_4^{2-}$  intercalated graphite flakes.<sup>42</sup> Through a high-speed air convection shearing treatment (Fig. S1e–g) process, the expanded graphite flakes can be transferred into multilayer graphene, and about 2.5 kg of multilayer graphene can be produced per hour through this proposed process.

Figure 1a displays a photograph of a bottle of the as-obtained multilayer graphene with a mass of 120 g. Figures 1b, c respectively, exhibit the low and high magnification SEM images of the as-obtained multilayer graphene collected from Fig. 1a, indicating that a large number of nanosheets with lateral size in the range of several hundreds of nanometers to tens of micrometers are obtained. In addition, the thickness of the as-obtained nanosheets is very thin as shown in the high magnification SEM (Fig. 1c), which can be further verified by XRD, TEM and AFM analysis. After exfoliation, the XRD peak centered at  $2\theta = 44.5^\circ$  attributed to (101) plane of graphite disappears (Fig. S2a), revealing the decrease of the graphite flake thickness. The Raman spectrum (Fig. S2b) of the as-obtained multilayer graphene shows two prominent peaks centered at 1580 and 2685  $\text{cm}^{-1}$ , which can be, respectively, assigned to the G and 2D bands of the as-obtained multilayer graphene. This Raman spectrum is typical for graphene demonstrating the formation of the multilayer graphene.<sup>43</sup> The intensity ratio of  $I_G/I_{2D}$  is about 0.72, which is higher than that of 0.5 reported in the literature for the predominantly monolayer graphene.<sup>44</sup> This result indicates that the as-obtained products are multilayer graphene rather than predominantly monolayer structure. Also, a peak located at about 1350  $\text{cm}^{-1}$  corresponding to D band is observed. The intensity ratio of  $I_D/I_G$  is about 0.15, similar to that of commercial graphene ( $I_D/I_G = 0.14$ ).<sup>23</sup> Figure 1d shows the TEM image of the as-obtained multilayer graphene, also revealing that the as-obtained multilayer graphene has a thin thickness and is nearly transparent to the electron beam. The corresponding SAED pattern exhibits the characteristic sixfold symmetrical diffraction for graphene (inset in Fig. 1d), suggesting the exfoliated multilayer graphene is highly

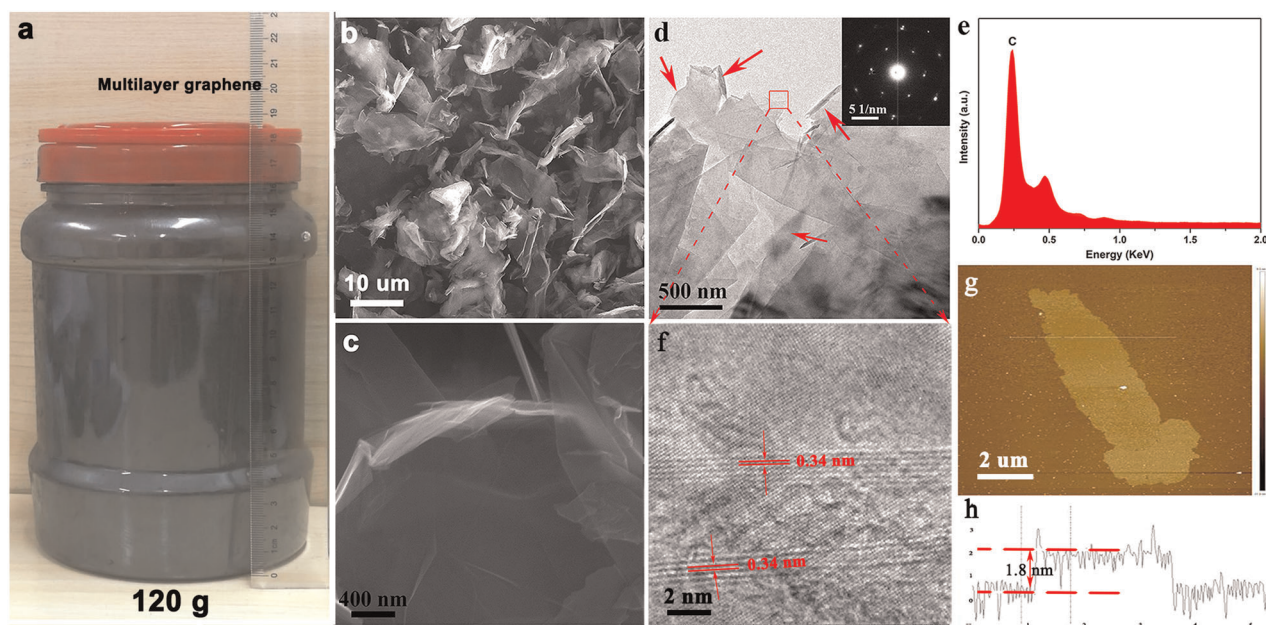


**Fig. 1** Characterization of the as-obtained multilayer graphene. **a** The photograph of a bottle of the as-obtained multilayer graphene with a mass of 120 g. **b**, **c** The low and high-magnification SEM images of the as-obtained multilayer graphene. **d** The low magnification TEM image of the as-obtained multilayer graphene. Inset is the corresponding SAED pattern. **e** The EDX spectrum of the as-obtained multilayer graphene. **f** The HRTEM image of the as-obtained multilayer graphene. **g** The AFM image and **h** corresponding height trace of a single multilayer graphene

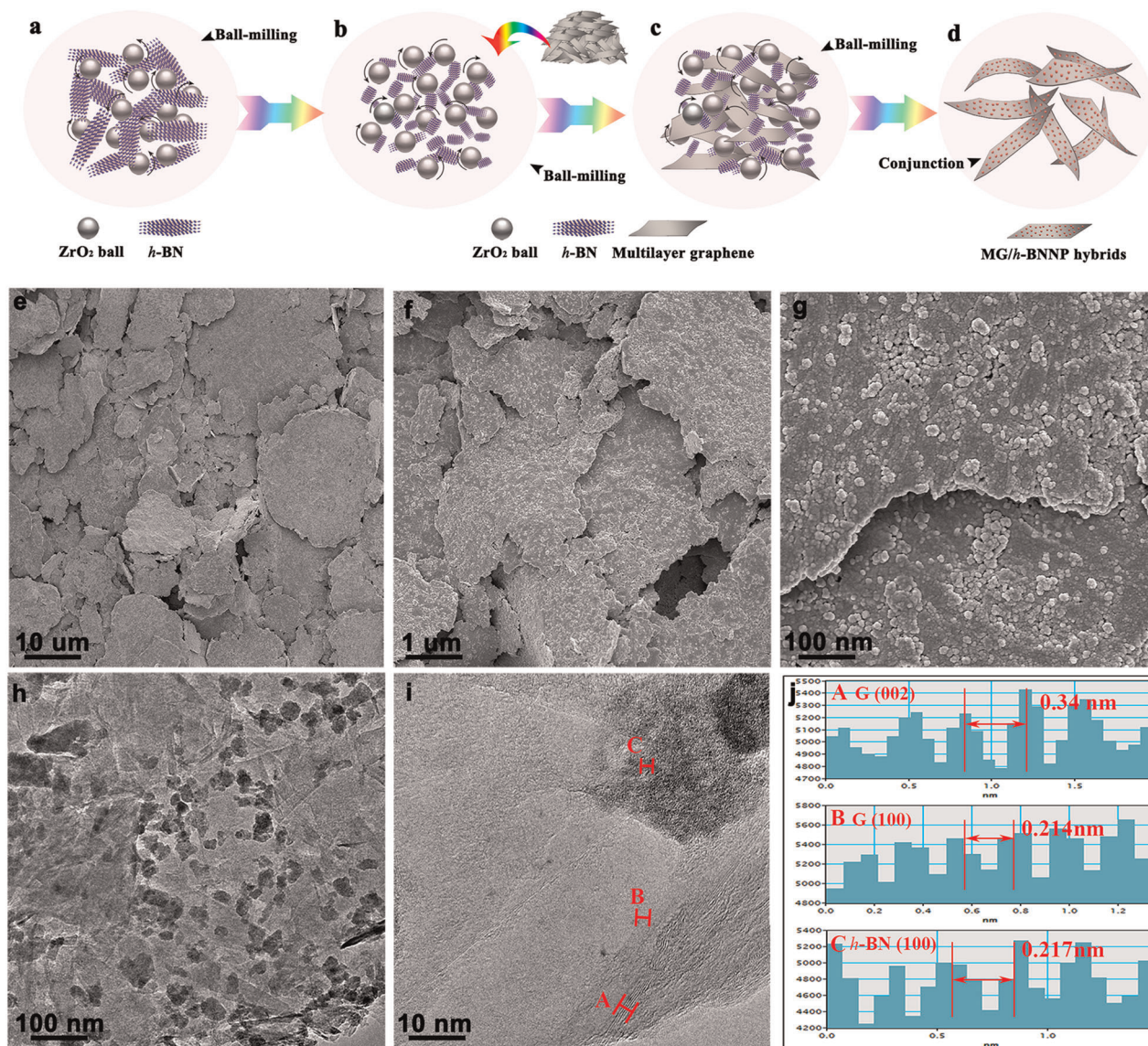


**Fig. 2** Preparation and characterization of the as-obtained MG/h-BNNP hybrids. **a–d** Schematic illustration for the preparation of the MG/h-BNNP hybrids. **e–g** The low and high-magnification SEM images of the as-obtained MG/h-BNNP-40%, showing that *h*-BNNPs are randomly distributed on the as-obtained multilayer graphene surfaces. **h, i** The TEM and HRTEM images of the as-obtained MG/h-BNNP-40%. **j** The corresponding distance profiles of **A, B,** and **C** in **i**, showing three kinds of spacing distance

crystalline. Generally, the edges of the as-obtained multilayer graphene are prone to be folded as marked in Fig. 1d (red arrow), allowing us to directly measure the number of the layers by HRTEM.<sup>45</sup> Figure 1f depicts the corresponding HRTEM image of the as-obtained multilayer graphene marked in Fig. 1d, showing that the as-obtained multilayer graphene is a typical five to six-layered structure with a thickness of about 2 nm. The average distance between adjacent fringes is 0.34 nm, corresponding to the intrinsic (002) plane spacing of graphite. The EDX (Fig. 1e) and XPS (Fig. S3) spectra demonstrate that the as-obtained multilayer graphene is mainly composed of carbon, showing high purity. The thickness of the as-obtained multilayer graphene can also be estimated by AFM analysis as shown in Fig. 1g, in which a typical rather flat nanosheet can be observed. The thickness of this flat sheet is about 1.8 nm calculated from the height trace profile as shown in Fig. 1h. In addition, the thickness distribution of the as-obtained multilayer graphene is evaluated by AFM (Fig. S4), showing that the thickness of the as-obtained multilayer graphene is relatively thin, mainly concentrated in 1.0–2.5 nm. In summary,

the massive preparation of high-quality graphene can be achieved by this proposed process, which is beneficial to the subsequent large scale preparation of the MG/h-BNNP hybrids.

#### Fabrication and characterization of MG/h-BNNP hybrids

The MG/h-BNNP hybrids were fabricated via a facile ball milling (QM-QX-2, MITR, China) process with the as-obtained multilayer graphene and commercial *h*-BN powders (average lateral size: 10 μm) as precursors (Fig. 2a–d). The *h*-BN powders were firstly ball milled for 35 h (Fig. 2a) and then the as-obtained multilayer graphene with different mass ratios to *h*-BNNPs was added (Fig. 2b). The ball milling process was continued for another 5 h (Fig. 2c, d) to prepare MG/h-BNNP hybrids. The MG/h-BNNP hybrids with different *h*-BNNP contents are named MG/h-BNNP-10%, MG/h-BNNP-20%, MG/h-BNNP-30%, MG/h-BNNP-40%, MG/h-BNNP-50%, and MG/h-BNNP-60%, respectively. It is noteworthy that the preparation of the hybrids can be scaled up to a large scale which is only limited by the volume of the ball milling jars. All the as-obtained MG/h-BNNP hybrids possess low densities less than

0.45 g/cm<sup>3</sup> (Fig. S5), and the densities increase with the increment of *h*-BNNP contents in the hybrids. The lowest density can be obtained from the MG/*h*-BNNP-10%, which is 0.294 ± 0.013 g/cm<sup>3</sup>.

Figure 2e shows the low magnification SEM image of the MG/*h*-BNNP-40%, revealing that the lamellar structure of the multilayer graphene is well retained. However, many nanoparticles can be observed attached to the surfaces of MG comparing with the previous as-obtained multilayer graphene (Fig. 1c). Through the ball milling pretreatment process, the *h*-BN flakes (Fig. S6a) will be ground into the *h*-BN nanoparticles (Fig. S6b) with the diameters in the range of several to tens of nanometers. In addition, the thicknesses of the *h*-BN nanoparticles are also significantly reduced, mainly concentrating at around 3 nm (Fig. S7). After a further ball milling treatment, the *h*-BNNPs will anchor on the surfaces of the as-obtained graphene, and the amount of the nanoparticles increases with the increment of the *h*-BNNP contents in the hybrids (Fig. S8). Figure 2f, g exhibit the magnified SEM images of the MG/*h*-BNNP-40%, in which a large number of nanoparticles with diameter in the range of several to tens of nanometers can be seen randomly distributed on the surface of the as-obtained graphene. Figure 2h displays the low magnification TEM image of the MG/*h*-BNNP-40%, further demonstrating that numerous nanoparticles with a diameter in the range of several to tens of nanometers are randomly anchored on the surfaces of the as-obtained graphene. This result coincides with that obtained by the SEM analysis. Figure 2i describes the HRTEM image of the MG/*h*-BNNP-40%, in which a small particle with a diameter of about 20 nm can be observed. Three kinds of spacing distance between adjacent fringes can be found from the HRTEM image as marked with A, B, and C, and the corresponding spacing distance is illustrated in Fig. 2j. The spacing distance of 0.34 and 0.214 nm can be, respectively, assigned to the (002) and (100) planes of graphite (JCPDS card No.41-1487), while the other one of 0.217 nm calculated from the particle corresponds to the (100) plane of *h*-BN (JCPDS card No. 34-0421). The crystalline structure of the *h*-BNNPs, ball milled multilayer graphene and the as-obtained MG/*h*-BNNP hybrids are further investigated by XRD analysis (Fig. S9), revealing that the crystalline structure of the as-obtained multilayer graphene is not destroyed completely during

the ball milling process since the two main diffraction peaks at  $2\theta = 26.5^\circ$  and  $54.7^\circ$  can be clearly observed. Interestingly, some weak peaks appear closing to the (002) peaks (Fig. S9, marked with X), which may be caused by the formation of the hybrids. In addition, the element mapping of the MG/*h*-BNNP-40% (Fig. S10) exhibits a uniform dispersion of C, B, and N elements, demonstrating that the *h*-BNNPs are randomly anchored on the surface of the as-obtained multilayer graphene to form the MG/*h*-BNNP hybrids.

#### Microwave absorption properties of the MG/*h*-BNNP hybrids

The microwave absorption properties of the as-obtained multilayer graphene, ball milled multilayer graphene, and MG/*h*-BNNP hybrids are calculated on the basis of the following equations<sup>46</sup>:

$$RL(dB) = 20 \log \left| \frac{Z_{in} - 1}{Z_{in} + 1} \right| \quad (1)$$

$$Z_{in} = \sqrt{\frac{\mu_r}{\epsilon_r}} \tan h \left[ j \left( \frac{2\pi f d}{c} \right) \sqrt{\mu_r \epsilon_r} \right] \quad (2)$$

where  $\epsilon_r$  ( $\epsilon_r = \epsilon' - j\epsilon''$ ) and  $\mu_r$  ( $\mu_r = \mu' - j\mu''$ ) are the complex permittivity and complex permeability of microwave absorption materials.  $Z_{in}$ ,  $f$ ,  $d$ , and  $c$  represent the impedance of free space, the frequency of the electromagnetic microwaves, the thickness of the absorber, and the velocity of electromagnetic wave in vacuum,<sup>47</sup> respectively.

The microwave absorption performance of *h*-BN, as-obtained multilayer graphene, ball milled multilayer graphene and MG/*h*-BNNP hybrid with different *h*-BNNP contents-based absorbers with the same loading rate of 30% was calculated according to Eqs. (1) and (2) as shown in Figs. 3, S11, and S12. Here, it is noteworthy that the loading rate of 30% is the optimized result through a series evaluation on the microwave absorption performance of the MG/*h*-BNNP hybrid based absorbers with different loading rates (Supporting information, Figs. S13–S15). Obviously, *h*-BN based absorber has no microwave absorption property, which is microwave transparent with RL values over  $-0.25$  dB (Fig. S11). Among the as-obtained multilayer graphene,

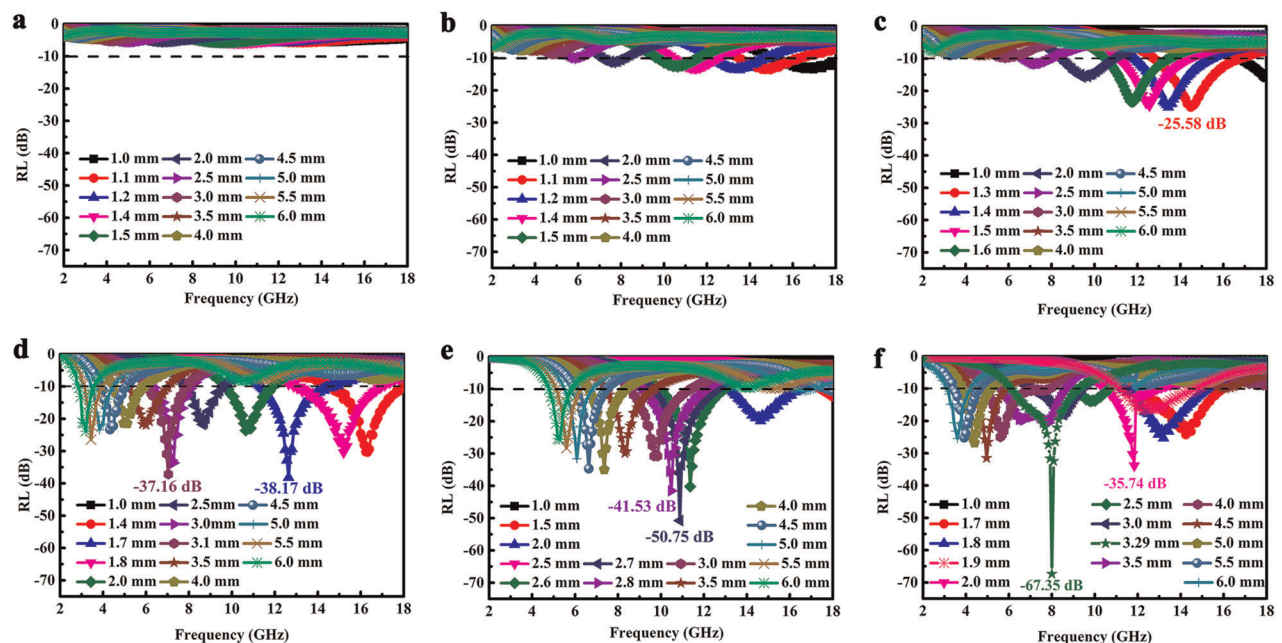


**Fig. 3** Evaluation of the microwave absorption properties of the samples. The minimum RL values for (a) the as-obtained multilayer graphene based absorber, (b) ball milled multilayer graphene based absorber, (c) the MG/*h*-BNNP-10% based absorber, (d) the MG/*h*-BNNP-20% based absorber, (e) the MG/*h*-BNNP 30% based absorber, and (f) the MG/*h*-BNNP-40% based absorber

**Table 1.** Microwave absorption performance comparison of the MG/h-BNNP-40% based absorber with recently representative work

Materials	wt. %	Minimum RL (dB)	Thickness (mm)	References
3D RGO framework	4.1	-36.0	3.3	5
3D graphene network	1	-43.5	3.5	9
Graphene@SiC aerogel	100	-47.3	3.0	18
Graphene flowers	10	-42.9	4.0	23
rGO/a-Fe <sub>2</sub> O <sub>3</sub> composite hydrogel	82	-33.5	5.0	58
Graphene/Fe <sub>3</sub> O <sub>4</sub> @Fe/ZnO	20	-38.4	5.0	59
3D RGO/ZnO	10	-25	2.5	60
RGO/Fe <sub>3</sub> O <sub>4</sub>	40	-27	2.0	61
3D RGO/ZnO	3.3	-27.8	4.8	62
MG/h-BNNP-40%	<b>30</b>	<b>-67.35</b>	<b>3.29</b>	<b>This work</b>

The bold value indicates the experimental data are obtained in our current work

ball milled multilayer graphene and MG/h-BNNP hybrid with different *h*-BNNP contents-based absorbers, the as-obtained multilayer graphene based absorber has the poorest microwave absorption performance and all the minimum RL values are more than -7.5 dB with the absorber thickness of 0.1–6.0 mm in the measurement frequency range of 2–18 GHz (Figs. 3 and S12a). After ball milling, the microwave absorption performance of the as-obtained multilayer graphene based absorber becomes better and the minimum RL values can reach up to -13.76 dB at 11.02 GHz when the absorber thickness is 1.4 mm (Figs. 3b and S12b). However, the microwave absorption properties of the MG/h-BNNP hybrid with different *h*-BNNP contents-based absorbers are further improved due to the existence of the *h*-BNNPs. The minimum RL values increase with the increment of *h*-BNNP contents in the hybrids as demonstrated in Fig. 3c–f and Fig. S12. The minimum RL values of the MG/h-BNNP-10%, MG/h-BNNP-20%, MG/h-BNNP-30%, MG/h-BNNP-40%, MG/h-BNNP-50%, and MG/h-BNNP-60% based absorbers can reach up to -25.58, -38.17, -50.75, -67.35, -19.31, and -30.15 dB, respectively. Distinctly, the MG/h-BNNP hybrid with the *h*-BNNP content of 40 wt.% possesses the best microwave absorption properties, and a minimum RL value of -67.35 dB can be obtained at 8.04 GHz when the thickness of the absorber is 3.29 mm. This microwave absorption performance is superior to most of the graphene or reduced graphene oxide based microwave absorption materials reported in the literatures (Table 1). In addition, the minimum RL values shift to high frequency region with the increase of the absorber thickness from 0.1 to 6.0 mm, indicating that the microwave absorption performance of the MG/h-BNNP hybrid based absorbers can be conveniently tuned by adjusting the thickness of the absorbers.

The RL value below -10 dB is a critical feature for the microwave absorption materials which possess good microwave absorption performance, since this RL value represents the absorption efficiency of 90% for electromagnetic microwaves.<sup>48</sup> When the RL value is below -20 dB, the absorption of the electromagnetic microwaves can reach up as high as 99%, suggesting an excellent absorption.<sup>49</sup> All the minimum RL values of the as-obtained multilayer graphene based absorber are greater than -6 dB (Fig. S16a) in the frequency range of 2–18 GHz, while the ones of the ball milled multilayer graphene based absorber show a little decrease which can reach -10 to -13 dB in the frequency range of 8–18 GHz with the absorber thickness in the range of 1.0–2.5 mm (Fig. S16b). However, the minimum RL values of the MG/h-BNNP hybrid with different *h*-BNNP contents-based absorbers are greatly improved, which can exceed -20 dB in a wide frequency range (Fig. S16c–f). The minimum RL values of the MG/h-BNNP-10% based absorber below -20 dB are mainly from

11.0 to 18.0 GHz with the absorber thickness of 1.0–2.0 mm (Fig. S16c). For the MG/h-BNNP-20% based absorber, the minimum RL values below -20 dB can be mainly observed from 3.0 to 18.0 GHz with the absorber thickness of 1.0–6.0 mm (Fig. S16d). When the *h*-BNNP content in the hybrids increases to 30%, the minimum RL values of the absorber below -20 dB can be found from 3.8 to 15.0 GHz with the absorber thickness of 1.5–5.5 mm (Fig. S16e). For the MG/h-BNNP-40% based absorber, the minimum RL values of the absorber below -20 dB can be, respectively, discovered in the frequency range of 3.3 to 10.5 GHz and 14.0 to 18.0 GHz with the absorber thickness of 1.0–6.0 mm (Fig. S16f). These results indicate that the MG/h-BNNP hybrids have an excellent capability to efficiently absorb electromagnetic microwaves in a wide frequency range. These excellent microwave absorption properties combining with the low densities make the g MG/h-BNNP hybrids very promising candidates for practical microwave absorption application.

## DISCUSSION

According to Eqs. (1) and (2), the microwave absorption performance of a microwave absorption material is highly associated with its complex permittivity ( $\epsilon_r = \epsilon' - j\epsilon''$ ) and complex permeability ( $\mu_r = \mu' - j\mu''$ ). Here,  $\epsilon'$  and  $\epsilon''$  can be, respectively, described as following equations in terms of Debye theory<sup>50</sup>:

$$\epsilon' = \epsilon_\infty + \frac{\epsilon_s - \epsilon_\infty}{1 + \omega^2\tau^2} \quad (3)$$

$$\epsilon'' = \frac{\epsilon_s - \epsilon_\infty}{1 + \omega^2\tau^2} \omega\tau + \frac{\sigma_{ac}}{\omega\epsilon_0} \quad (4)$$

where  $\epsilon_s$ ,  $\epsilon_\infty$ ,  $\omega$ ,  $\tau$ ,  $\sigma_{ac}$ , and  $\epsilon_0$ , respectively, represent static permittivity, relative dielectric permittivity at the high-frequency limit, angular frequency, polarization relaxation time, alternative conductivity, and dielectric constant in vacuum ( $\epsilon_0 = 8.854 \times 10^{-12} \text{ F}\cdot\text{m}^{-1}$ ).<sup>50,51</sup> Based on Eq. (3), the variation of  $\epsilon'$  values in the frequency range of 2–18 GHz is associated with the change of  $\omega\tau$ , which can be regarded as polarization relaxation in different frequency.<sup>51</sup> And for the  $\epsilon''$ , it could be deduced into Eq. (5) on the basis of the free electron theory<sup>52</sup>:

$$\epsilon'' = \frac{1}{2} \epsilon_0 \pi \rho f \quad (5)$$

where  $\epsilon_0$  is the permittivity of a vacuum,  $\rho$  is the resistivity,  $f$  is the frequency of the microwave. The Eq. (5) indicates that the  $\epsilon''$  values are highly associated with the electrical conductivity of a microwave absorption material.

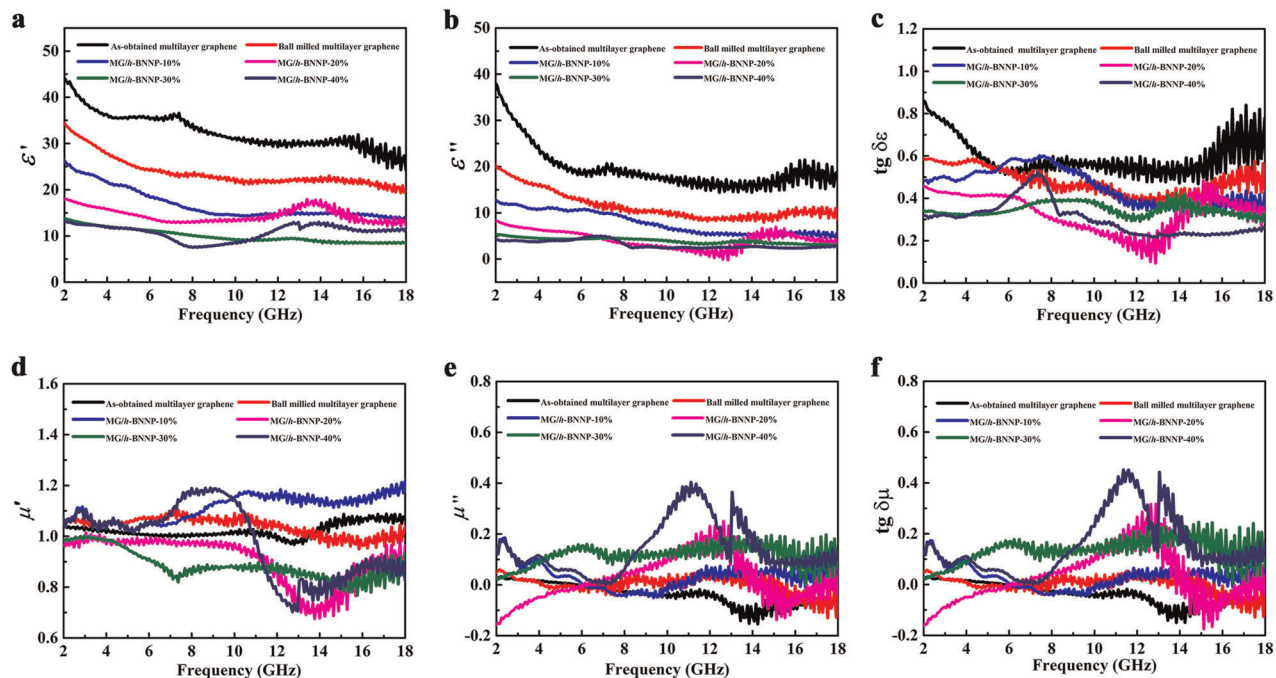


**Fig. 4** Characterization of the electromagnetic parameters of the samples. **a, b** Frequency dependences of real part ( $\epsilon'$ ) and imaginary part ( $\epsilon''$ ) of the complex permittivity. **c** Frequency dependences of the dielectric loss. **d, e** Frequency dependences of real part ( $\mu'$ ) and imaginary part ( $\mu''$ ) of the complex permeability. **f** Frequency dependences of the magnetic loss

Figure 4a, b show the  $\epsilon'$  and  $\epsilon''$  values of the as-obtained multilayer graphene, ball milled multilayer graphene and MG/h-BNNP hybrid with different h-BNNP contents-based absorbers with the same loading rate of 30 wt.% in the frequency range of 2–18 GHz. Obviously, the as-obtained multilayer graphene based absorber has the highest  $\epsilon'$  and  $\epsilon''$  values which, respectively, change in the range of 25–45 and 15–40 over the frequency range of 2–18 GHz (Fig. 4a, b). After ball milling, the  $\epsilon'$  and  $\epsilon''$  values of the ball milled multilayer graphene based absorber, respectively, decrease to 20–35 and 10–20. This decrease of  $\epsilon'$  and  $\epsilon''$  values can be ascribed to the formation of the defective structure during the ball milling process.<sup>23</sup> The  $\epsilon'$  and  $\epsilon''$  values of the MG/h-BNNP hybrid with different h-BNNP contents based absorbers will further decrease which are, respectively, below 25 and 13 due to the existence of h-BNNPs. The attached h-BNNPs can cover a large amount of freely migrated electrons and will hinder the other free migrated electron migration path. The decrease of the freely migrated electrons and electron migration path will lead to the decrease of the polarization relaxation of MG/h-BNNP hybrids when the frequency changes, resulting in the decrease of  $\epsilon'$  values since the  $\epsilon'$  values are highly associated with the polarization relaxation in different frequency. In addition, the  $\epsilon''$  values are highly associated with the electrical conductivity of a microwave absorption material. The as-obtained multilayer graphene has excellent crystal structure which will give them excellent electrical conductivity. The random distribution of the as-obtained multilayer graphene in paraffin can create an electrically conductive network even at very low concentration according to the threshold theory,<sup>53</sup> resulting in good electrical conductivity. When the h-BNNPs are introduced, the ordered freely migrated electron distribution is destroyed, leading to the degradation of the electrical conductivity. Besides, the amount and contacting area of multilayer graphene will decrease in the conductive network due to the existence of the large quantities of h-BNNPs which will further decrease the electrical conductivity (Fig. S17 and S18). Although, the microwave cannot be efficiently attenuated when  $\epsilon'$  and  $\epsilon''$  values are low, over high  $\epsilon'$  and  $\epsilon''$  values are also harmful for microwave absorption.<sup>23</sup> On one hand, over high  $\epsilon'$  and  $\epsilon''$

values will lead to the mismatch between air and absorber interface, resulting in more electromagnetic microwaves are reflected in the interface. On the other hand, high  $\epsilon''$  values will lead to a high leakage current and skin effect,<sup>53–55</sup> which may cause damage to the electromagnetic microwave absorption. Herein, one of the reasons for the MG/h-BNNP hybrids showing excellent microwave absorption properties can be assigned to the optimization of  $\epsilon'$  and  $\epsilon''$  values.

Previous research also demonstrates that Debye dipolar relaxations have an important influence on  $\epsilon'$  and  $\epsilon''$  values of microwave absorption materials, which can be described by Cole-Cole semicircle. Based on the Eqs. (3) and (4), the relationship between  $\epsilon'$  and  $\epsilon''$  can be deduced as Eq. (6)

$$(\epsilon' - \epsilon_\infty)^2 + (\epsilon'')^2 = (\epsilon_s - \epsilon_\infty)^2 \quad (6)$$

The curve of  $\epsilon' - \epsilon''$  would be a single semicircle, generally defined as a Cole-Cole semicircle, and each semicircle corresponds to a Debye dipolar relaxation.<sup>53</sup> Figure 5 shows the dielectric Cole-Cole semicircle of the as-obtained multilayer graphene, ball milled multilayer graphene and MG/h-BNNP hybrid with different h-BNNP contents-based absorbers in the frequency range of 2–18 GHz. Obviously, only one Cole-Cole semicircle can be found in the  $\epsilon' - \epsilon''$  curves of the as-obtained multilayer graphene and ball milled multilayer graphene (Fig. 5a, b) based absorbers, indicating the existence of a small number of Debye relaxation process in the as-obtained multilayer graphene and ball milled multilayer graphene based absorbers. Meanwhile, 3, 3, 3, and 4 semicircles are clearly observed in the curves of the MG/h-BNNP-10%, MG/h-BNNP-20%, MG/h-BNNP-30%, and MG/h-BNNP-40% based absorbers, respectively (Fig. 5c–f), suggesting that more Debye relaxation exists in the MG/h-BNNP hybrid based absorbers. The appearance of more Debye relaxation will also enhance the microwave absorption properties of the MG/h-BNNP hybrids.

Figure 4d and e present the  $\mu'$  and  $\mu''$  values of the as-obtained multilayer graphene, ball milled multilayer graphene and MG/h-BNNP hybrid with different h-BNNP contents based absorbers with the same loading rate of 30 wt.% in the frequency range of 2–18 GHz. The  $\mu'$  and  $\mu''$  values for the as-obtained multilayer

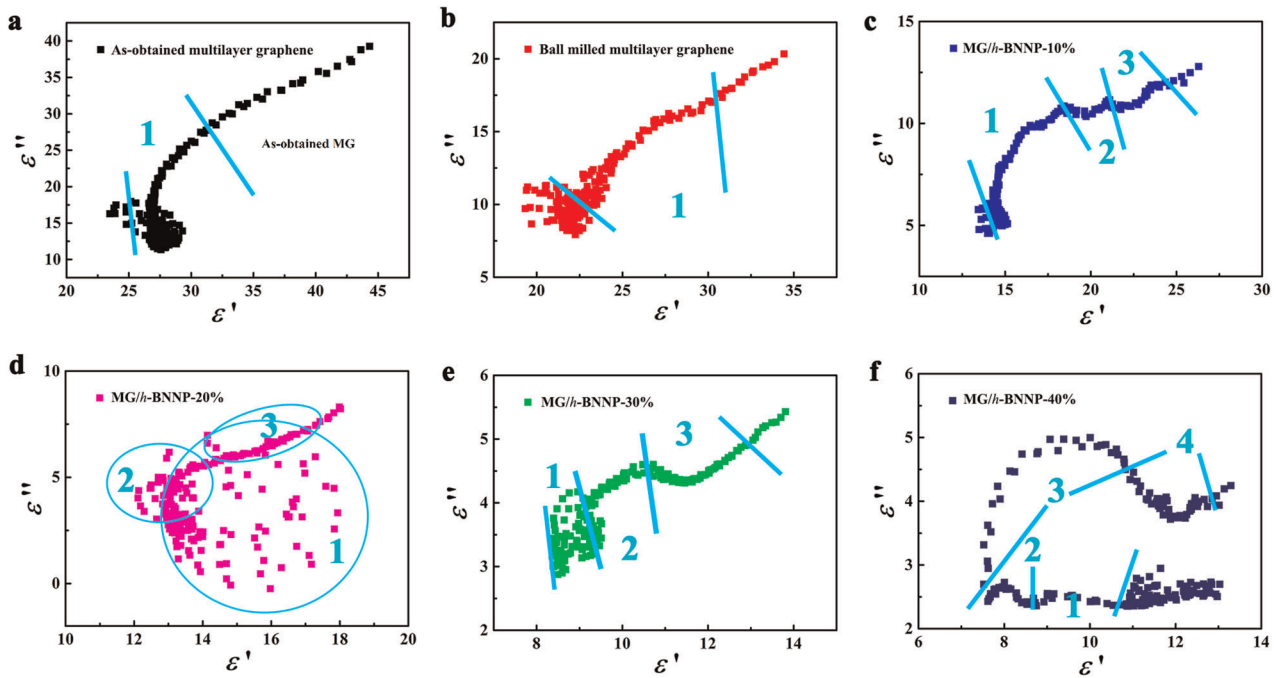


**Fig. 5** The  $\epsilon'$ – $\epsilon''$  curves of the samples. **a** the as-obtained multilayer graphene, **b** ball milled multilayer graphene, **c** MG/h-BNNP-10%, **d** MG/h-BNNP-20%, **e** MG/h-BNNP-30%, and **f** MG/h-BNNP-40% based absorbers

graphene and ball milled multilayer graphene based absorbers are close to 1 and 0, indicating that they have no magnetism. However, after formation of the MG/h-BNNP hybrids, the  $\mu''$  values exhibit slight increase as the *h*-BNNP contents increase in the hybrids, which are beneficial to improve the microwave absorption performance. Strangely, the  $\mu'$  values of the hybrids only show more dramatic fluctuations as the *h*-BNNP contents increase in the hybrids. These results indicate that the introduction of *h*-BNNPs onto multilayer graphene surfaces can improve the magnetic properties of the MG/h-BNNP hybrids. To verify the change of the magnetic properties of the MG/h-BNNP hybrids, the magnetic properties of the as-obtained multilayer graphene, ball milled multilayer graphene and MG/h-BNNP hybrids with different *h*-BNNP contents are measured. The as-obtained multilayer graphene has almost no magnetism in accordance with the results of  $\mu'$  and  $\mu''$  values (Fig. S19). Although the magnetism is still very weak for all the MG/h-BNNP hybrids, it shows a slight increase with the increment of *h*-BNNP contents in the hybrids (Fig. S19). Here, the change of the polarization will also affect the magnetism of the MG/h-BNNP hybrids since the magnetism of a material is also closely associated with their polarization property. Because of the variation of the polarization, there will be a lag of the polarization over the time when frequency change, thus leading to the appearance of the weak magnetism. Herein, the appearance of this weak magnetism is another reason for enhancing the microwave absorption properties of the MG/h-BNNP hybrids.

For further probing the microwave absorption mechanism of the MG/h-BNNP hybrid based absorbers, the dielectric ( $tg\delta_\epsilon = \epsilon''/\epsilon'$ ) and magnetic ( $tg\delta_\mu = \mu''/\mu'$ ) loss of the as-obtained multilayer graphene, ball milled multilayer graphene and MG/h-BNNP hybrid with different *h*-BNNP contents based absorbers are also calculated as displayed in Fig. 4c and f. The  $tg\delta_\epsilon$  values of the MG/h-BNNP hybrid with different *h*-BNNP contents based absorbers exhibit a slight decrease compared to those of the as-obtained and ball milled multilayer graphene based absorbers. However, the  $tg\delta_\mu$  values increase due to the increase of the  $\mu''$  values. It is well accepted that the dielectric and magnetic loss represent the capability of microwave absorption materials to

convert electromagnetic microwave to other forms of energy, and high dielectric and magnetic losses are beneficial for microwave absorption.<sup>23</sup> Here, the multilayer graphene based absorber with the highest dielectric loss fails to produce the best microwave absorption property because there is another parameter also influences the microwave absorption property of a microwave absorption material which is impedance matching ( $Z_{in}$ ).

On the basis of Eq. (1), when  $Z_{in}$  is closer to 1, the incident microwave could achieve zero reflection at the front surface of the microwave absorption absorbers, and this will result in perfect electromagnetic microwave absorption.<sup>56,57</sup> Therefore, for further investigating the microwave absorption mechanism, the impedance matching of the as-obtained multilayer graphene, ball milled multilayer graphene and MG/h-BNNP hybrid with different *h*-BNNP contents based absorbers are calculated as shown in Fig. 6. Clearly, the as-obtained multilayer graphene based absorber shows the worst impedance matching, which is below 0.3 with the absorber thickness from 0.1 to 6.0 mm in the frequency range of 2–18 GHz (Fig. 6a). As a result, the as-obtained multilayer graphene based absorber exhibits the poorest microwave absorption performance (Fig. 3a). After ball milling, the impedance matching of the ball milled multilayer graphene based absorber is slightly improved which increases to about 0.7 with the absorber thickness from 0.9 to 2.5 mm in the frequency range of 6–18 GHz (Fig. 6b). Correspondingly, the microwave absorption property of the ball milled multilayer graphene based absorber is a little bit enhanced with the absorber thickness from 0.9 to 2.5 mm in the frequency range of 6–18 GHz (Fig. 3b). For the MG/h-BNNP hybrid with different *h*-BNNP contents based absorbers, the impedance matching is greatly improved as demonstrated in Fig. 6c–f. For the MG/h-BNNP-10% based absorber, the best impedance matching appears in the frequency range of 10–18 GHz with the absorber thickness from 1.0 to 2.0 mm. Correspondingly, the minimum RL values which are less than –20 dB can be observed in this region (Fig. 3c). The best impedance matching of the MG/h-BNNP-20% based absorber appears in the frequency range of 3.0–18.0 GHz with the absorber thickness from 1.2 to 6.0 mm. As a result, the minimum RL values which are less than –20 dB can be found in this region (Fig. 3d).

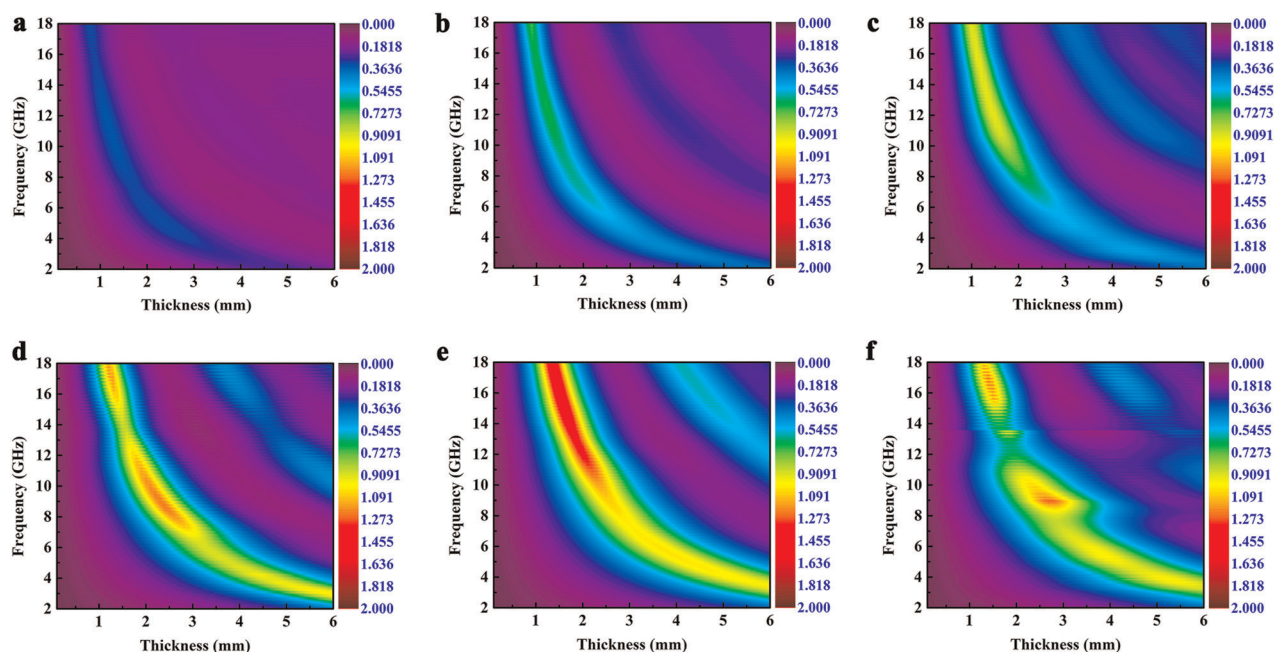


**Fig. 6** The 2D maps of the relationship between Zin and Z0 of the samples. **a** the as-obtained multilayer graphene, **b** ball milled multilayer graphene, **c** MG/h-BNNP-10%, **d** MG/h-BNNP-20%, **e** MG/h-BNNP-30%, and **f** MG/h-BNNP-40% based absorbers

For the MG/h-BNNP-30% based absorber, the best impedance matching appears in the frequency range of 4–12 GHz with the absorber thickness from 2.5 to 6.0 mm. Accordingly, the minimum RL values which are less than  $-20$  dB can be observed in this region (Fig. 3e). The best impedance matching of the MG/h-BNNP-40% based absorber appears in the frequency range of 3–10 and 14–18 GHz with the absorber thickness from 2.0 to 6.0 mm. Coincidentally, the minimum RL values which are less than  $-20$  dB can be observed in this region.

In summary, the multilayer graphene with the size of several nanometers in thickness and several hundreds of nanometers to tens of micrometers in lateral size can be massively fabricated through a facile oxidation-thermal expansion-air convection shearing process with natural graphite flakes as precursors. The introduction of *h*-BNNPs can effectively tune the dielectric and magnetic properties of this multilayer graphene. Correspondingly, the microwave absorption properties of these MG/h-BNNP hybrid based absorbers are significantly enhanced. The MG/h-BNNP hybrid with *h*-BNNP content of 40 wt.% shows the best microwave absorption property with a minimum RL value of  $-67.35$  dB at 8.04 GHz when the absorber thickness is 3.29 mm and loading rate is 30 wt.% in the absorber. The enhancement of the microwave absorption performance of the MG/h-BNNP hybrid based absorbers can be assigned to two reasons. On one hand, the formation of the MG/h-BNNP hybrids can reduce the dielectric property and improve the magnetic property of multilayer graphene to optimize impedance matching. On the other hand, the formation of the MG/h-BNNP hybrids can increase the contact interface thus improving the interfacial polarization effects. Moreover, the MG/h-BNNP hybrids possess low densities which are less than  $0.45$  g/cm<sup>3</sup>, making them very attractive for practical microwave absorption application.

## METHODS

### Mass fabrication of multilayer graphene

Before fabrication, the expandable graphite was prepared by the method reported in the literature.<sup>31</sup> Generally, the expandable graphite was fabricated by using H<sub>2</sub>SO<sub>4</sub>-graphite intercalation composite, which could yield a high expansion volume *via* thermal treatment. Typically, the natural

graphite flakes (Fig. S1a, Dongguan Jiecheng graphite Co., Ltd.), H<sub>2</sub>SO<sub>4</sub> (98 wt.%) and H<sub>2</sub>O<sub>2</sub> (30 wt.%) were mixed uniformly and reacted for 90 min at 50 °C (Fig. S1b). After the reaction, the products were collected and washed to neutral with water. SO<sub>4</sub><sup>2-</sup> intercalated graphite flakes can be obtained (Fig. S1c) after dried at 60 °C in an oven. The as-obtained SO<sub>4</sub><sup>2-</sup> intercalated graphite flakes were then subjected to a thermal treatment in a furnace at 700 °C for a duration of 15 min (Fig. S1d). This thermal treatment condition has been demonstrated an effective way for complete expansion of SO<sub>4</sub><sup>2-</sup> intercalated graphite flakes.<sup>32</sup> Finally, the expanded graphite flakes (Fig. S1e) were transferred into a home-made high-speed air convection shearing equipment for exfoliation (Fig. S1f, g).

### Fabrication of MG/h-BNNP hybrids

The MG/h-BNNP hybrids were fabricated via a facile ball milling (QM-QX-2, MITR, China) process with the as-obtained multilayer graphene and commercial *h*-BN powders (average lateral size: 10 μm) as precursors (Fig. 2a–d). Typically, commercial *h*-BN powders (0.1, 0.2, 0.3, 0.4, 0.5, 0.6 g) (zirconia balls: 3/5 mm = 100/50 g) were firstly ball milled for 35 h with a rotation speed of 300 rpm to preparation *h*-BNNPs (Fig. 2a). Then, the as-obtained multilayer graphene (0.9, 0.8, 0.7, 0.6, 0.5, 0.4 g) was added into the jars and continued the ball milling for another 5 h (Fig. 2b). The MG/h-BNNP hybrids with different *h*-BNNP contents can be obtained when the ball milling process terminated (Fig. 2c). The MG/h-BNNP hybrids with different *h*-BNNP contents are, respectively, named MG/h-BNNP-10%, MG/h-BNNP-20%, MG/h-BNNP-30%, MG/h-BNNP-40%, MG/h-BNNP-50%, and MG/h-BNNP-60%. Importantly, the preparation scale of these hybrids can be scaled up which is limited by the volume of the ball mill jars. For comparison, the as-obtained multilayer graphene was also ball milled for 5 h for microwave absorption property measurement.

### Materials characterization

The XRD spectra were carried out on X' PERT PRO X-ray diffractometer with Cu K $\alpha$  radiation ( $\lambda = 0.154178$  nm). Raman spectrum was recorded on a Reni Shaw Raman spectrometer operating at 532 nm. The SEM images were collected on JSM 6701F scanning electron microscope. The TEM and HRTEM images were obtained on FEI Tecnai G2 F30 transmission electron microscope equipped with EDX system. The AFM analysis was conducted on Smart SPM (AIST-NT) atomic force microscope.

### Electromagnetic parameter measurements

The magnetic properties of the as-obtained multilayer graphene, ball milled multilayer graphene and MG/h-BNNP hybrids were investigated



with a VSM magnetometer from Quantum Design. The microwave absorption performance of *h*-BN, the as-obtained multilayer graphene, ball milled multilayer graphene and MG/*h*-BNNP hybrid based absorbers was evaluated by a vector network analyzer (VNA; Agilent N5245A) in transmission-reflection mode in the frequency range of 2–18 GHz. The power level of the incident microwave radiation used for the measurements is –15 dBm. During the measurement process, paraffin was selected as dispersant to make the measurement samples due to its good processability and nearly zero RL of microwave. The samples were prepared by uniformly mixing of *h*-BN, the as-obtained multilayer graphene, ball milled multilayer graphene and MG/*h*-BNNP hybrids with paraffin, and then the mixtures were pressed into toroidal shaped samples with inner diameter of 3.04 mm, outer diameter of 7.0 mm, and thickness of 3.0 mm.

## DATA AVAILABILITY

All data related to the paper is available on request from the corresponding authors.

## ACKNOWLEDGEMENTS

This work was supported by the Foundation of Lanzhou Institute of Chemical Physics, the National Natural Science Foundation of China (51875550, 51527901, 51872058, U1737213), the Youth Innovation Promotion Association (2017459), and the Science and Technology Program of Gansu Province (18JR3RA380).

## AUTHOR CONTRIBUTIONS

Y.L.Y., Y.Q.B., and J.Y.Z. conceived the project; Y.L.Y., Y.Q.B., B.Z., and J.Y.Z. designed the experiments; B.Z., M.W., and C.Y.W. prepared the multilayer graphene; Y.Q.B., Y.L.Y., and B.Z. carried out the MG/*h*-BNNP hybrids fabrication; Y.Q.B., M.W., A.M.L., and K.X.G. performed the material characterization; Y.L.Y. and Y.Q.B. wrote the paper; All authors contributed to analysis of the data and discussions of results.

## ADDITIONAL INFORMATION

**Supplementary Information** accompanies the paper on the *npj 2D Materials and Applications* website (<https://doi.org/10.1038/s41699-019-0115-5>).

**Competing interests:** The authors declare no competing interests.

**Publisher's note:** Springer Nature remains neutral with regard to jurisdictional claims in published maps and institutional affiliations.

## REFERENCES

- Brzozowski, M. et al. The research of modern radar equipment conducted in the air force institute of technology by the application of military aircrafts. *Avi. Adv. Mainten.* **40**, 26–45 (2017).
- Neri, B. et al. Advances in technologies, architectures, and applications of highly-integrated low-power radars. *IEEE Aero. El. Sys. Mag.* **27**, 25–36 (2012).
- Singh, A. P. et al. Encapsulation of  $\gamma$ -Fe<sub>2</sub>O<sub>3</sub> decorated reduced graphene oxide in polyaniline core-shell tubes as an exceptional tracker for electromagnetic environmental pollution. *J. Mater. Chem. A* **2**, 3581–3593 (2014).
- Ding, Y. et al. Electromagnetic wave absorption in reduced graphene oxide functionalized with Fe<sub>3</sub>O<sub>4</sub>/Fe nanorings. *Nano. Res.* **9**, 2018–2025 (2016).
- Song, W. L. et al. Strong and thermostable polymeric graphene/silica textile for lightweight practical microwave absorption composites. *Carbon* **100**, 109–117 (2016).
- Estrada, D. et al. Thermal transport in layer-by-layer assembled polycrystalline graphene films. *NPJ 2D Mater. Appl.* **3**, 10 (2019).
- Akhtar, M. et al. Recent advances in synthesis, properties, and applications of graphophore. *NPJ 2D Mater. Appl.* **1**, 5 (2017).
- Geim, A. K. Graphene: status and prospects. *Science* **324**, 1530–1534 (2009).
- Liu, W. et al. Fabrication of ultralight three-dimensional graphene networks with strong electromagnetic wave absorption properties. *J. Mater. Chem. A* **3**, 3739–3747 (2015).
- Novoselov, K. S. et al. Electric field effect in atomically thin carbon films. *Science* **306**, 666–669 (2004).
- Suk, J. W. et al. Transfer of CVD-grown monolayer graphene onto arbitrary substrates. *ACS Nano* **5**, 6916–6924 (2011).
- Sun, Z. Z. et al. Growth of graphene from solid carbon sources. *Nature* **468**, 549–552 (2010).

- Hernandez, Y. et al. High-yield production of graphene by liquid-phase exfoliation of graphite. *Nat. Nanotechnol.* **3**, 563–568 (2008).
- Kosynkin, D. V. et al. Longitudinal unzipping of carbon nanotubes to form graphene nanoribbons. *Nature* **458**, 872–876 (2009).
- Kosynkin, D. V. et al. Highly conductive graphene nanoribbons by longitudinal splitting of carbon nanotubes using potassium vapor. *ACS Nano* **5**, 968–974 (2011).
- Dreyer, D. R. et al. The chemistry of graphene oxide. *Chem. Soc. Rev.* **39**, 228–240 (2009).
- Han, M. K. et al. Flexible and thermostable Graphene/SiC nanowire foam composites with tunable electromagnetic wave absorption properties. *ACS Appl. Mater. Interfaces* **9**, 11803–11810 (2017).
- Jiang, Y. et al. Lightweight spongy bone-like graphene@SiC aerogel composites for high-performance microwave absorption. *Chem. Eng. J.* **337**, 522–531 (2018).
- Qu, B. et al. Coupling hollow Fe<sub>3</sub>O<sub>4</sub>-Fe nanoparticles with graphene sheets for high-performance electromagnetic wave absorbing material. *ACS Appl. Mater. Interfaces* **8**, 3730–3735 (2016).
- Sun, D. et al. Controlled synthesis of porous Fe<sub>3</sub>O<sub>4</sub>-decorated graphene with extraordinary electromagnetic wave absorption properties. *Acta Mater.* **61**, 5829–5834 (2013).
- Yan, F. et al. An ultra-small NiFe<sub>2</sub>O<sub>4</sub> hollow particle/graphene hybrid: fabrication and electromagnetic wave absorption property. *Nanoscale* **10**, 2697–2703 (2018).
- Ren, Y. et al. Three-dimensional SiO<sub>2</sub>@Fe<sub>3</sub>O<sub>4</sub> core/shell nanorod array/graphene architecture: synthesis and electromagnetic absorption properties. *Nanoscale* **5**, 12296–12303 (2013).
- Chen, C. et al. Porous graphene microflowers for high-performance microwave absorption. *Nano-Micro Lett.* **10**, 26 (2018).
- Li, L. H. et al. Atomically thin boron nitride: unique properties and applications. *Adv. Funct. Mater.* **26**, 2594–2608 (2016).
- Falin, A. et al. Mechanical properties of atomically thin boron nitride and the role of interlayer interactions. *Nat. Commun.* **8**, 15815 (2017).
- Lin, C. H. et al. A flexible solar-blind 2D boron nitride nanopaper-based photo-detector with high thermal resistance. *NPJ 2D Mater. Appl.* **2**, 23 (2018).
- Li, L. H. et al. Strong oxidation resistance of atomically thin boron nitride nanosheets. *ACS Nano* **8**, 1457–1462 (2014).
- Liu, Z. et al. Ultrathin high-temperature oxidation-resistant coatings of hexagonal boron nitride. *Nat. Commun.* **4**, 2541 (2013).
- Yu, Y. et al. Superhydrophobic and superoleophilic porous boron nitride nanosheet/polyvinylidene fluoride composite material for oil-polluted water cleanup. *Adv. Mater. Interfaces* **2**, 1400267 (2015).
- Zhong, B. et al. Three dimensional hexagonal boron nitride nanosheet/carbon nanotube composites with light weight and enhanced microwave absorption performance. *Compos. Part. A. Appl.* **112**, 515–524 (2018).
- Zhu, H. et al. Highly thermally conductive papers with percolative layered boron nitride nanosheets. *ACS Nano* **8**, 3606–3613 (2014).
- Bai, Y. et al. Ball milling of hexagonal boron nitride microflakes in ammonia fluoride solution gives fluorinated nanosheets that serve as effective water-dispersible lubricant additives. *ACS Appl. Nano. Mater.* **2**, 3187–3195 (2019).
- Watanabe, K. et al. Direct-bandgap properties and evidence for ultraviolet lasing of hexagonal boron nitride single crystal. *Nat. Mater.* **3**, 404 (2004).
- Laturia, A. et al. Dielectric properties of hexagonal boron nitride and transition metal dichalcogenides: from monolayer to bulk. *NPJ 2D Mater. Appl.* **2**, 6 (2018).
- Woessner, A. et al. Electrical detection of hyperbolic phonon-polaritons in heterostructures of graphene and boron nitride. *NPJ 2D Mater. Appl.* **1**, 25 (2017).
- Khorasani, S. et al. Nonlinear graphene quantum capacitors for electro-optics. *NPJ 2D Mater. Appl.* **1**, 7 (2017).
- Fan, M. et al. Doping nanoscale graphene domains improves magnetism in hexagonal boron nitride. *Adv. Mater.* **31**, 1805778 (2019).
- Yin, J. et al. Boron nitride nanostructures: fabrication, functionalization and applications. *Small* **12**, 2942–2968 (2016).
- Akman, N. et al. Island shape, size and interface dependency on electronic and magnetic properties of graphene hexagonal-boron nitride (*h*-BN) in-plane hybrids. *J. Phys. Chem. Solids* **115**, 187–198 (2018).
- Bediako, D. K. et al. Heterointerface effects in the electrointercalation of van der Waals heterostructures. *Nature* **558**, 425 (2018).
- Xia, L. et al. Preparation and thermal characterization of expanded graphite/paraffin composite phase change material. *Carbon* **48**, 2538–2548 (2010).
- Zhang, P. et al. Composite reactive block for heat transformer system and improvement of system performance. *J. Chem. Eng. Jpn.* **40**, 1275–1280 (2007).
- Ferrari, A. C. et al. Raman spectrum of graphene and graphene layers. *Phys. Rev. Lett.* **97**, 187401 (2006).
- Ma, L. et al. Transparent conducting graphene hybrid films to improve electromagnetic interference (EMI) shielding performance of graphene. *ACS Appl. Mater. Interfaces* **9**, 34221–34229 (2017).

45. Wang, X. et al. "Chemical Blowing" of thin-walled bubbles: high-throughput fabrication of large-area, few-layered BN and C-x-BN Nanosheets. *Adv. Mater.* **23**, 4072–+ (2011).
46. Miles, P. A. et al. Dielectric spectroscopy of ferromagnetic semiconductors. *Rev. Mod. Phys.* **29**, 279–307 (1957).
47. Qing, Y. et al. Epoxy-silicone filled with multi-walled carbon nanotubes and carbonyl iron particles as a microwave absorber. *Carbon* **48**, 4074–4080 (2010).
48. Quan, L. et al. Dielectric and microwave absorption properties of polymer derived SiCN ceramics annealed in N-2 atmosphere. *J. Eur. Ceram. Soc.* **34**, 589–598 (2014).
49. Kang, Y. et al. Incorporate boron and nitrogen into graphene to make BCN hybrid nanosheets with enhanced microwave absorbing properties. *Carbon* **61**, 200–208 (2013).
50. Wu, F. et al. Reduced graphene oxide (RGO) modified spongelike polypyrrole (PPy) aerogel for excellent electromagnetic absorption. *J. Mater. Chem. A* **3**, 14358–14369 (2015).
51. Wang, Y. F. et al. Hybrid of MoS<sub>2</sub> and reduced graphene oxide: a lightweight and broadband electromagnetic wave absorber. *ACS Appl. Mater. Interfaces* **7**, 26226–26234 (2015).
52. Xu, P. et al. Synthesis of electromagnetic functionalized nickel/polypyrrole core/shell composites. *J. Phys. Chem. B* **112**, 10443–10448 (2008).
53. Zhang, X. J. et al. Polymer-composite with high dielectric constant and enhanced absorption properties based on graphene-CuS nanocomposites and polyvinylidene fluoride. *J. Mater. Chem. A* **1**, 12115–12122 (2013).
54. Wang, T. et al. Graphene-Fe<sub>3</sub>O<sub>4</sub> nanohybrids: synthesis and excellent electromagnetic absorption properties. *J. Appl. Phys.* **113**, 024314 (2013).
55. Cooper, E. R. et al. Ionic liquids and eutectic mixtures as solvent and template in synthesis of zeolite analogues. *Nature* **430**, 1012–1016 (2004).
56. Cui, C. et al. Synthesis of electromagnetic functionalized Fe<sub>3</sub>O<sub>4</sub> microspheres/polyaniline composites by two-step oxidative polymerization. *J. Phys. Chem. B* **116**, 9523–9531 (2012).
57. Du, Y. et al. Shell thickness-dependent microwave absorption of core-shell Fe<sub>3</sub>O<sub>4</sub>@C composites. *ACS Appl. Mater. Interfaces* **6**, 12997–13006 (2014).
58. Zhang, H. et al. Novel rGO/α-Fe<sub>2</sub>O<sub>3</sub> composite hydrogel: synthesis, characterization and high performance of electromagnetic wave absorption. *J. Mater. Chem. A* **1**, 8547–8552 (2013).
59. Ren, Y. L. et al. Quaternary nanocomposites consisting of graphene, Fe<sub>3</sub>O<sub>4</sub>@Fe Core@Shell, and ZnO nanoparticles: synthesis and excellent electromagnetic absorption properties. *ACS Appl. Mater. Interfaces* **4**, 6436–6442 (2012).
60. Wu, F. et al. Two-step reduction of self-assembled three-dimensional (3D) reduced graphene oxide (RGO)/zinc oxide (ZnO) nanocomposites for electromagnetic absorption. *J. Mater. Chem. A* **2**, 20307–20315 (2014).
61. Sun, X. et al. Laminated magnetic graphene with enhanced electromagnetic wave absorption properties. *J. Mater. Chem. C* **1**, 765–777 (2013).
62. Song, C. et al. Three-dimensional reduced graphene oxide foam modified with ZnO nanowires for enhanced microwave absorption properties. *Carbon* **116**, 50–58 (2017).



**Open Access** This article is licensed under a Creative Commons Attribution 4.0 International License, which permits use, sharing, adaptation, distribution and reproduction in any medium or format, as long as you give appropriate credit to the original author(s) and the source, provide a link to the Creative Commons license, and indicate if changes were made. The images or other third party material in this article are included in the article's Creative Commons license, unless indicated otherwise in a credit line to the material. If material is not included in the article's Creative Commons license and your intended use is not permitted by statutory regulation or exceeds the permitted use, you will need to obtain permission directly from the copyright holder. To view a copy of this license, visit <http://creativecommons.org/licenses/by/4.0/>.

© The Author(s) 2019